Microstructure and mechanical properties of high-Mn-ODS steels

S. Seils[a,b], A. Kauffmann[a,], W. Delis[a], T. Boll[a,b] and M. Heilmaier[a]*

[a] Institute for Applied Materials (IAM-WK), Karlsruhe Institute of Technology (KIT), Engelbert-Arnold-Str. 4, D-76131 Karlsruhe, Germany

[b] Karlsruhe Nano Micro Facility (KNMF), Karlsruhe Institute of Technology (KIT), Hermann-von-Helmholtz-Platz 1, D-76344 Eggenstein-Leopoldshafen, Germany

**corresponding author*

mail: alexander.kauffmann@kit.edu, phone: +4972160842346

Abstract

The contribution of dislocation density to strength of Cr-Ni containing austenitic ODS steels is assumed to be limited by dynamic recovery during consolidation of mechanically alloyed powder [Seils et al., Materials Science and Engineering A 786 (2020) 139452]. In order to prevent the reduction in dislocation density by dislocation annihilation subsequent to thermally activated cross slip during recovery, Cr and Ni were replaced by 24 and 34 wt.% of Mn in the present study. The comparably lower stacking fault energy leads to larger stacking fault widths and, hence, lower probability of cross slip. The Mn-ODS steels were successfully manufactured by mechanical alloying and subsequent field assisted sintering. X-ray diffraction analysis revealed increased dislocation densities for both Mn-ODS alloys compared to a previously reported Cr-Ni-ODS steel. Formation of additional ε-phase was observed in the lower Mn alloy. Compression and hardness tests confirmed an improved strength and hardness of the Mn-ODS steels. Less thermal stability was found compared to the Cr-Ni-ODS steels due to pronounced ripening of oxide particles as well as grain coarsening in both investigated alloys.

Keywords

ODS steel; high-Mn steel; mechanical alloying; microstructure characterization; strengthening mechanisms.

1. Introduction

Oxide dispersion strengthened (ODS) steels are promising materials for application at elevated temperatures. Originally, ferritic ODS steels were introduced as possible candidates for cladding materials in future nuclear fission and fusion power plants [1–3] for which among others the high corrosion resistance [4–6], the high resistance against irradiation caused swelling [7–10] and superior creep resistance compared to common high temperature steels [1,2,11] were decisive. In recent years, the interest in austenitic ODS steels increased [12–16]. Due to their close-packed, face-centered cubic (FCC) crystal structure, they are expected to provide even higher creep strength in comparison to their ferritic counterparts in the high temperature range above 600 °C [14,17].

The extraordinary properties of ODS steels are mainly related to nano-scaled oxides, so-called nanoclusters, usually less than 4 nm in size [18–22]. To obtain a homogenous distribution of these nanoclusters in the material, mechanical alloying (MA) of yttria powder with elemental or pre-alloyed metallic powders and subsequent consolidation by hot extrusion [1,2,23], hot isostatic pressing (HIP) [20,21], or field assisted sintering technique (FAST) [16,24,25] are typically applied. In contrast to hot extrusion or HIP, FAST allows for short consolidation times, which prevent coarsening of grains and/or ripening of nano-scaled oxides during consolidation and leads to equiaxed, ultra-fine grains without preferential orientation.

The strength of ODS steels depends on several strengthening mechanisms [14,26–28]. In our previous work [16], we compared the strengthening contributions of a ferritic (Fe-14Cr-0.4Ti-0.25Y_2O_3 in wt.%) and an austenitic Cr-Ni-ODS steel (Fe-25Cr-20Ni-0.4Ti-0.25Y_2O_3 in wt.%, designated as *austenitic RT* in what follows). Hall-Petch strengthening (due to the ultrafine grain size), Orowan strengthening (due to the nanoclusters hindering dislocation motion) as well as dislocation strengthening (due to the relatively high dislocation density because of the MA process) were identified as main strengthening contributions. However, the strength obtained for *austenitic RT*, reached only about 50% of the strength of the ferritic counterpart [16] which was rationalized by a lower Hall-Petch coefficient (0.3 MPa · $m^{1/2}$ [29] compared to 0.6 MPa · $m^{1/2}$ [30] for the ferritic ODS steel) as well as a lower dislocation density after consolidation by FAST. Since the dislocation density of both ODS steel variants were concurrently in the range of 10^{16} m^{-2} immediately after MA, a seemingly different amount of recovery and/or recrystallization during consolidation is supposed to be responsible for the lower dislocation density of the austenitic ODS steel. To improve its strength, it is believed difficult, if not impossible, to increase the Hall-Petch contribution σ_{HP} which depends on the grain size d_{g} and the Hall-Petch coefficient k_{HP} (see eq. (1)).

$$\sigma_{\mathrm{HP}} = \frac{k_{\mathrm{HP}}}{\sqrt{d_{\mathrm{g}}}} \tag{1}$$

d_{g} was already in the range of a few hundred nanometers and k_{HP} is a constant which does not vary substantially within the same materials group.

A promising way to improve the strength may, thus, be to increase the dislocation density of the consolidated material by deliberately manipulating the tendency to recover or recrystallize. Reduced probability of recovery is expected for materials with lower stacking fault energy, in which the distance between Shockley partial dislocations is higher and, hence, the constriction prior to cross-slip requires stronger fluctuations. For the Cr-Ni-containing ODS steel *austenitic RT* [16], the experimentally determined SFE is about 45 to 55 mJ/m² [31,32].

Austenitic steels in which the SFE can be manipulated over a wide range are high-Mn steels. Experimental results [33–40] and theoretical assessments [41–43] on the SFE in the binary Fe-Mn-system and in various Fe-Mn-based alloys have shown that high-Mn-containing ODS steels are expected to exhibit a significantly lower SFE than austenitic Cr-Ni-containing ODS steels. However, recovery also takes place during severe plastic deformation of the powders. Thus, an increased driving force for recrystallization during consolidation may also be expected.

Besides the SFE, the possible formation of the hexagonal close-packed (HCP) ε-phase is another criterion for the alloy design when considering Mn-containing steels. Binary Fe-Mn alloys exhibit at least fractions of ε-phase at Mn concentrations between 10 and 28 wt.%, while no ε-phase was found at Mn concentrations above 30 wt.% [44–46]. Furthermore, the formation of ε-phase also depends on

64 the grain size of the material, i.e. no ε-phase was observed in Mn-containing steels with grain size
65 below 1 µm [47]. Since Mn-containing ODS steels are manufactured by MA, the limited grain size and
66 the severely deformed microstructure will influence the phase formation.
67 To the authors' best knowledge, there exists only a single report by Ashong et al. [48] so far dealing
68 with the mechanical properties of a Fe-25Mn-0.4Ti-0.2C-0.4Y_2O_3 (in wt.%) ODS steel, manufactured by
69 HIP and additional hot rolling at 1150 °C, in comparison to a ferritic ODS steel of the same composition
70 without Mn. The authors obtained ε- and γ-phase in the Mn-containing steel and identified nano-
71 scaled oxides of $Y_2Ti_2O_7$-type (< 30 nm in size) and $TiMn_2O_4$-type up to 180 nm in size by means of
72 transmission electron microscopy (TEM) [48]. There is no information provided about the phase
73 formation as a function of Mn content. The authors have also shown that high dislocation densities of
74 about 10^{15} m^{-2} can in general be achieved in Mn-containing ODS steels but no direct comparison to
75 austenitic ODS steels with higher SFE manufactured under the same conditions was conducted [48].
76 In contrast to this previous work, we investigate for the first time the influence of the Mn-content and,
77 hence, the SFE on the microstructural and mechanical properties of austenitic ODS steels in the as-
78 milled and consolidated condition. Two Mn-containing ODS steels with 24 and 34 wt.% Mn were
79 consolidated at temperatures ranging from 1000 to 1100 °C by FAST. We aim at increasing the
80 dislocation density and strength of high-Mn-ODS steels in comparison to Mn-free, Cr-Ni-based,
81 austenitic ODS steels [16], which were processed in a similar way. Furthermore, we focus on the phase
82 and cluster formation and thermal stability dependent on (i) Mn content and (ii) the consolidation
83 temperature.

2. Materials and methods

All ODS steels investigated in this work were manufactured by powder metallurgical processing. The nominal compositions (in wt.%) of the Mn-containing ODS steels were Fe-24Mn-0.4Ti-0.25Y_2O_3 (designated as "*24Mn*" in further discussion) and Fe-34Mn-0.4Ti-0.25Y_2O_3 ("*34Mn*"), respectively. Elemental powders (30 g in total) of Fe, Mn and Ti (Alfa Aesar, purity of 99.2 wt.% or higher, size < 45 µm), Y_2O_3 (size < 10 µm) and steel balls (10 mm in diameter) with a ball-to-powder ratio of 10:1 were filled in steel milling jars under protective Ar atmosphere. MA was performed in a PM400 planetary ball mill (Retsch GmbH) for 2880 cycles of 60 s milling at 200 rpm and 120 s cooling without rotation (48 h net milling time). Rotation was reversed after each cycle. Prior to consolidation, all powders of one batch but from different milling jars were mixed for 12 h at 200 rpm in Ar protective atmosphere in the planetary ball mill. Analyses on powders of both alloys are indicated by the addition of "*-MA*" to the alloy name in the following. A field assisted sintering furnace (machine type "HP D" by FCT Systeme GmbH) was used for subsequent consolidation of the powders in graphite dies of 20 mm in diameter. A holding time of 5 min at a pressure of 50 MPa was applied for the consolidation of the material at 1000, 1050 and 1100 °C (visualized by the addition of *"-1000*", "*-1050*" or "*-1100*" to the alloy designation). Stagnancy of the compression dies indicated completion of densification and the end of the sintering process. Heating and cooling rate were 100 $K \cdot min^{-1}$. Additional annealing at 1100 °C for 1 h (indicated by "-HT" in the sample nomenclature) with heating and cooling rate of 250 $K \cdot min^{-1}$ was performed in a vacuum tube furnace (STF by Carbolite Gero GmbH) for selected specimens.

For microstructural analyses, mechanically alloyed powders or parts of consolidated material were embedded in resin and prepared by standard metallographic procedure including grinding on SiC paper and subsequent polishing with diamond suspensions down to 1 µm. Surface-near deformation was finally removed by polishing with a non-crystallizing oxide suspension (pH = 9.8, Struers GmbH).

XRD analyses were performed on polished and rotating sections with the help of a D2 Phaser device (Bruker Corp.) equipped with a Cu X-ray source and a LynxEye line detector. To filter the fluorescence radiation of Fe, appropriate discriminator settings were used.

An Auriga 60 (Zeiss AG) scanning electron microscope was used for backscatter electron (BSE) imaging and electron backscatter diffraction (EBSD) analyses. BSE micrographs were taken at an acceleration voltage of 20 kV. For EBSD analyses, micrographic sections were mounted on 70° pre-tilted holders and investigated with acceleration voltage of 20 kV at working distances of 14 to 16 mm. A DigiView camera (EDAX Inc.) in combination with the TSL OIM Data Collection software (EDAX Inc.) was used to collect Kikuchi patterns. To identify grain boundaries, a minimum misorientation of 5° between neighboring pixels was used. Where necessary, orientation maps were cleaned by means of the

neighbor confidence index correlation method applied on data points with a confidence index less than 0.1.

Tips for atom probe tomography (APT) were manufactured exclusively from the *34Mn-1050* and the *34Mn-1050-HT* sample by a standard lift-out procedure in a combined SEM/focused ion beam device (Strata by FEI). APT analyses were performed in a LEAP 4000X HR device (Cameca SAS) equipped with a UV laser (wave length λ = 355 nm). Temperature, laser pulse energy, pulse repetition rate and detection rate were set to 50 K, 50 pJ, 200 kHz and 0.3% to 1%, respectively. 3D reconstruction of atom probe data was performed by means of the IVAS 3.6.14 software (Cameca SAS) and SEM profiles. Oxide particles were identified by the maximum separation method, which is described in detail elsewhere [49–51]. Y, YiO and TiO ions were used for the cluster identification. The necessary parameters for the identification of oxide particles were individually determined for each tip following the description of Williams et al. [20]. For *34Mn-1050*, the maximum separation distance $d_{\max}$ and the minimum number of ions per cluster $N_{\min}$ were in the range of 0.8 to 1.4 nm and 15 to 38, respectively, while $d_{\max}$ and $N_{\min}$ were in the range of 1.2 to 1.5 nm and 4 to 12 for *34Mn-1050-HT*, respectively. For further details on APT sample preparation and APT analysis procedure, the reader is referred to Ref. [16].

Characterization of mechanical properties was performed by means of hardness and compression tests at room temperature. A Q10A+ micro hardness device is used to determine the Vickers hardness on polished sections of powders as well as consolidated material. To make hardness tests on powder particles possible, a relatively low load of 0.02 N is used. 16 indents per condition were made with a loading time of 10 s each. Quasi-static compression tests (with initial strain rate of $\dot{\varepsilon} = 10^{-4}\ s^{-1}$) were performed in a Zwick 1478 universal testing device (Zwick GmbH). Cylindrical samples with an initial height and diameter of 5 and 3 mm, respectively, were manufactured by electrical discharge machining (EDM) and subsequently ground to obtain parallel load surfaces. BN spray was applied to the samples to reduce friction during testing and strain was determined by strain gauges attached to the compression dies in direct vicinity of the sample. At least 10% plastic strain was obtained in each test. Yield strength $\sigma_{0.2}$ was determined from the stress-strain curves at 0.2% plastic strain.

3. Results

3.1 Characterization of microstructure

After MA, the peaks in the diffraction patterns of both alloys can be assigned to the FCC phase (Cu prototype, see Figs. 1a & d). Additionally, *24Mn-MA* exhibits two low intensity peaks from the HCP ε-phase (Mg prototype, see Fig. 1a). After consolidation of *24Mn* at 1000 °C, no ε-peaks are visible (Fig. 1b), whereas the transformation from austenite to ε is clearly obtained after consolidation at 1100 °C (Fig. 1c). It can be concluded from Figs. 1d and e, that no ε-phase is formed in *34Mn* at all.

A modified Nelson-Riley approach [52] is used to precisely determine the lattice parameters. For *24Mn*, the lattice parameter of FCC austenite is (3.602 ± 0.036) Å for the mechanically alloyed powder, (3.601 ± 0.002) Å for *24Mn-1000* and (3.600 ± 0.004) Å for *24Mn-1100*. For ε-phase, found in *24Mn-1100* the lattice parameters are a = (2.540 ± 0.010) Å and c = (4.098 ± 0.010) Å. Due to the low intensity and the lack of higher order peaks, the lattice parameters of the ε-phase in *24Mn-MA* were not determined. For *34Mn-MA* and *34Mn-1100*, the FCC lattice parameter is (3.613 ± 0.019) Å and (3.612 ± 0.002) Å, respectively.

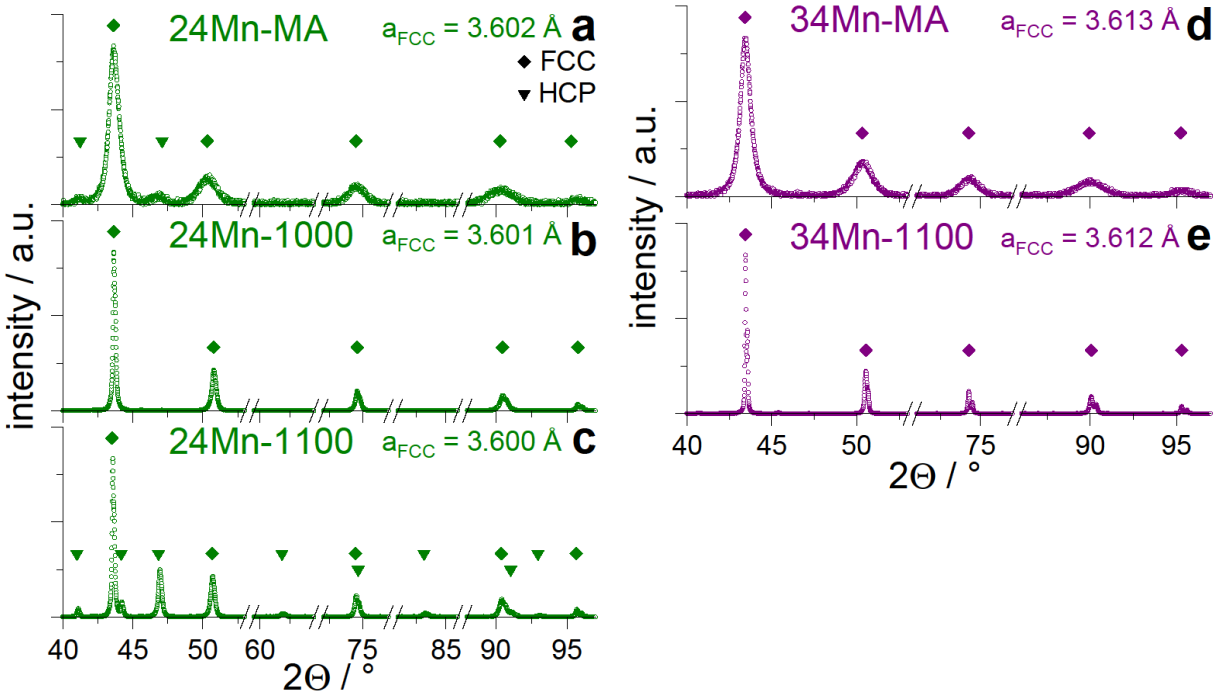

Figure 1: XRD patterns of *24Mn* (a-c) and *34Mn* (d and e) for the mechanically alloyed powder (a and d) as well as for the material consolidated at 1000 (b) and 1100 °C (c and f). Closed diamonds highlight FCC peak positions calculated from the given FCC lattice parameters. Closed triangles highlight peaks of the ε-phase calculated from the HCP lattice parameters a = 2.540 Å and c = 4.098 Å. For better visibility of the individual low intensity peaks and their peak shape, only relevant sections of 2Θ are plotted.

Dislocation densities in the austenitic phase of the mechanically alloyed powders as well as of the consolidated materials were estimated from E_{hkl}-normalized Williamson-Hall (WH) plots [53], which account for the elastic anisotropy of the material. E_{hkl} represents the orientation-specific Young's modulus of the individual set of lattice planes. Note that this approach considers that all lattice strains result from dislocations but due to its simplicity it provides a statistically relevant estimate on all portions of a phase within the material. This is a rough estimate in the present case due to stacking fault and ε-phase contributions to peak width of the austenite. For the determination of the peak width, deconvolution of the $K\alpha_1$ and $K\alpha_2$ contributions was conducted. Furthermore, in the case of *24Mn-1100*, peaks of the austenite which overlap with peaks from the ε-phase (Fig. 1c) are not used for the determination of dislocation density. However, the dislocation density is only marginally changed when considering these peaks as well. Resulting dislocation densities are summarized in Fig. 2.

Prior to consolidation, the dislocation densities of both Mn-containing alloys are in the order of 10^{16} m^{-2} due to severe plastic deformation. After consolidation at 1000 and 1050 °C the dislocation densities of both, *24Mn* and *34Mn* are in the range of about $3 – 6 \cdot 10^{14}$ m^{-2}. This is different for consolidation at 1100 °C. While the dislocation density of *24Mn-1100* remains at the same level as for lower consolidation temperatures, *34Mn-1100* exhibits a significant drop in dislocation density.

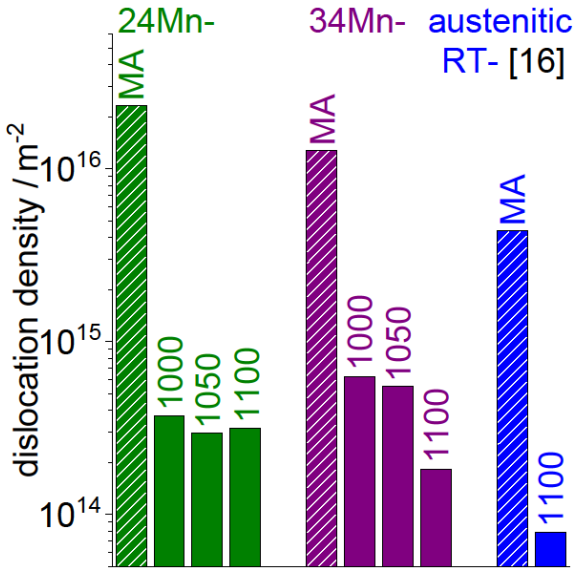

Figure 2: Dislocation density of *24Mn* and *34Mn* after MA as well as after consolidation at different temperatures (1000, 1050 and 1100 °C). As reference, the dislocation densities of Cr-Ni-ODS steel *austenitic RT* from Ref. [16] is also provided.

SEM micrographs show that material's density was not sufficient after consolidation at 1000 °C. Areal image analysis revealed porosity of up to 4 vol.% for *24Mn-1000* (Fig. S1a). Due to the significant porosity found in alloys consolidated at 1000 °C, these alloys are not further analyzed. Consolidation

at 1050 °C leads to a homogenous, fine-grained microstructure for both Mn-containing alloys and coarse grains being presumably aligned along former particle boundaries (see also Fig. S1) which is similar to the findings on *austenitic RT* in Ref. [16]. Grain sizes of consolidated alloys were determined by EBSD analysis. The area-averages of grain sizes of *24Mn-1050* and *34Mn-1050* were smaller than 0.5 µm and in the same order as for *austenitic RT* [16]. Larger grain sizes of (1.8 ± 1.3) µm (Fig. 3a) and (3.5 ± 2.0) µm were determined for *24Mn-1100* and *34Mn-1100*, respectively. EBSD analysis was also used to determine the phase fraction of ε-phase in *24Mn-1050* and *24Mn-1100* to be 18 and 56 vol.%, respectively. Fig. 3b shows the phase map for *24Mn-1100*, which proofs the significant proportion of ε-phase identified by Kikuchi patterns (example shown in Fig. 3c).

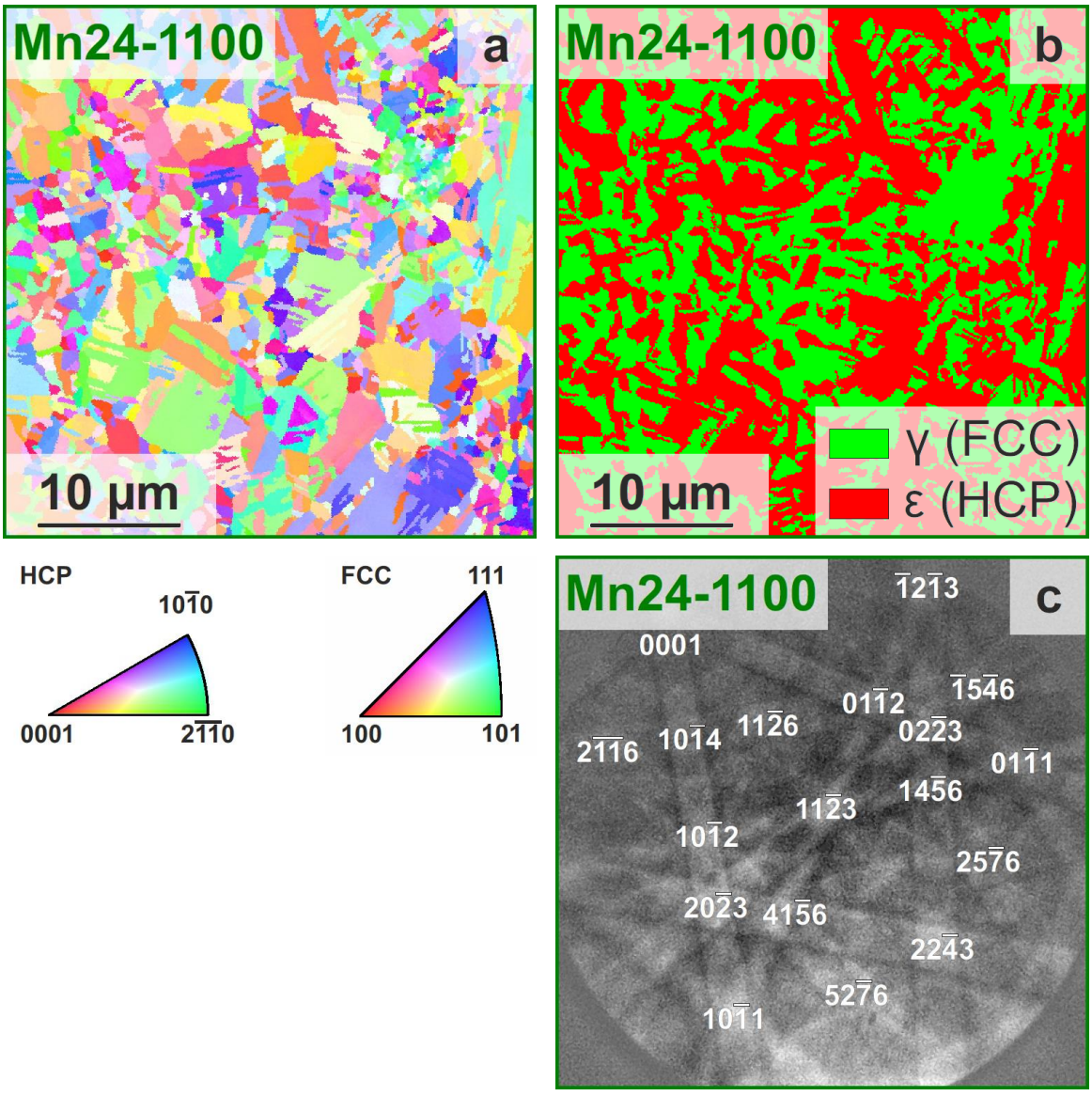

Figure 3: EBSD analysis of *24Mn-1100* showing a) the IPF map as well as b) the corresponding phase map, indicating γ- (green) and ε-phase (red); c) shows an example of the Kikuchi pattern for the identification of the ε-phase.

3.2 Thermal stability

IPF maps of *24Mn* and *34Mn* consolidated at 1050 °C are presented before (Figs. 4a and c) and after annealing for 1 h at 1100 °C (Figs. 4b and d) and reveal grain coarsening during annealing from below 0.5 µm to about (2.9 ± 2.0) µm and (3.2 ± 2.1) µm, respectively. In contrast to the materials consolidated at 1050 °C, no further grain coarsening was observed for *24Mn-1100-HT* and *34Mn-1100-HT*. Grain sizes after annealing are summarized in Tab. 1.

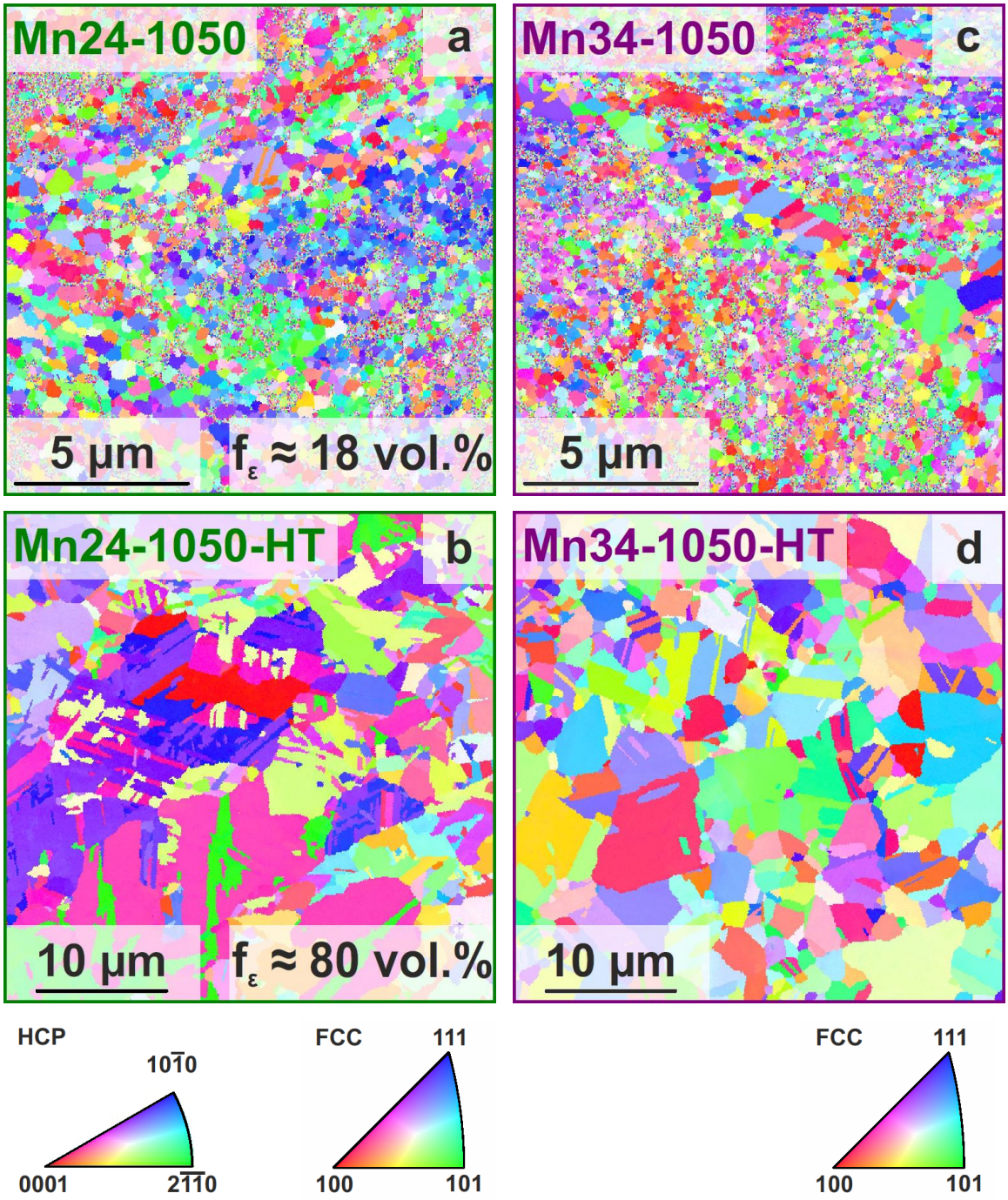

Figure 4: IPF maps of *24Mn-1050* (a & b) and *34Mn-1050* (c & d), before (a & c) and after annealing (b & d) for 1 h at 1100 °C.

In *24Mn-1050-HT*, the fraction of ε-phase increases from about 18 vol.% in the consolidated material to about 80 vol.% in the annealed material. Note here, that the fraction of ε-phase in *24Mn-1050* is an estimate due to the small grain size of this material and the necessary clean-up procedure. Further γ to ε transformation is also observed for *24Mn-1100* where the fraction of ε-phase increases from 56 vol.% (Fig. 3b) to 63 vol.% for *24Mn-1100* and *24Mn-1100-HT*, respectively. In the annealed samples *34Mn-1050-HT* and *34Mn-1100-HT* no ε-phase was observed at all.

To analyze the thermal stability of nanoclusters in the Mn-containing ODS steels, APT analyses of the fully austenitic *34Mn-1050* and *34Mn-1050-HT* samples were performed. Additional effects due to the γ-to-ε transformation can be excluded for *34Mn*. Fe and Mn ions were found to be homogenously distributed in the matrix. Figs. 5a and b show cross-sections of reconstructed APT tips (thickness of 20 nm) of *34-Mn-1050* and *34Mn-1050-HT*, respectively. For the sake of clarity, only ions enriched in particles are visualized here. Besides Y, Ti, O, YO and TiO, also MnO and FeO ions were determined within the particles. Hence, nanoclusters were found to contain a significant amount of Mn (about 12 at.% in average) and Fe (less than 5 at.% in average), even after matrix correction [20] of the nanocluster composition.

Although nanoclusters seem to be homogenously distributed in the presented APT tips, it should be noted that other samples contain regions free from nanoclusters. Nanoclusters, found in *34Mn-1050* have an average radius of gyration r_{NC} of (1.1 ± 0.9) nm and a particle density ρ_{NC} of $1.7 \cdot 10^{23}$ m^{-3}. During annealing of *34Mn-1050-HT* the nanocluster size increased significantly to r_{NC} = (2.1 ± 1.4) nm while the particle density decreased to $2.0 \cdot 10^{21}$ m^{-3}.

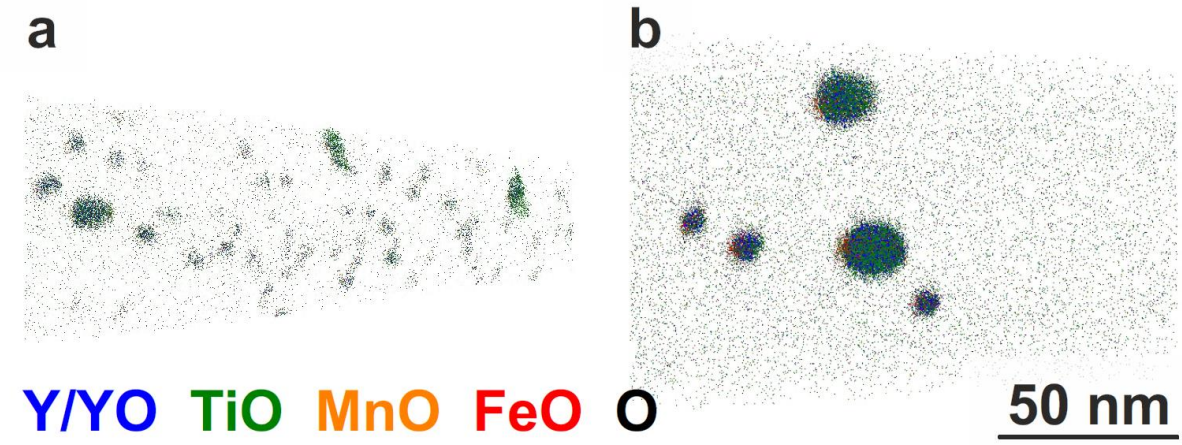

Figure 5: Reconstructed APT tips (20 nm thick slice) of *34Mn-1050* a) before and b) after annealing for 1 h at 1100 °C. Ion types which are not enriched in nanoclusters are omitted.

Table 1: Grain size (from IPF maps) and nanocluster size (from APT) after annealing for 1 h at 1100 °C.

specimen	grain size in µm	ε-fraction in vol.%	r_{NC} in nm	NC density in m^{-3}
24Mn-1050-HT	2.9 ± 2.0	80	–	–
24Mn-1100-HT	2.2 ± 1.6	63	–	–
34Mn-1050-HT	3.2 ± 2.1	0	2.1 ± 1.4	$2.0 \cdot 10^{21}$
34Mn-1100-HT	3.4 ± 2.1	0	–	–

211

3.3 Mechanical properties

212 Mechanical properties of the ODS steels were investigated by means of compression tests at room
213 temperature of *24Mn* and *34Mn* after consolidation at 1050 and 1100 °C. Since no compression tests
214 are possible on mechanically alloyed powders, Vickers hardness tests were also performed to enable
215 the comparison of powder and consolidated material. As reference, results of the *austenitic RT* alloy
216 from Ref. [16] are also provided. From hardness and yield strength of the various consolidated samples
217 a linear correlation of these two properties could be derived, following

$$\sigma_{\mathrm{ys}} = 2.9 \cdot HV0.02 - 278 \tag{2}$$

218 with adjusted R^2_{adj} = 0.95. In eq. (4), $HV0.02$ is the hardness value and σ_{ys} is the corresponding yield
219 strength in MPa. From Fig. 6, it can be concluded that the hardness of the mechanically alloyed
220 powders of *24Mn* and *34Mn* as well as of the *austenitic RT* alloy is about 850 to 900 HV0.02 which
221 corresponds to yield strength above 2 GPa.
222 Consolidation leads to a decrease in hardness as well as in yield strength of at least 50%. For *24Mn-*
223 *1050* and *34Mn-1050* the yield strength was (1081 ± 2) MPa and (1055 ± 5) MPa, respectively, which
224 is higher than the yield strenght of (916 ± 27) MPa for the reference alloy *austenitic RT* [16] (Fig. 6).
225 After consolidation at the same consolidation temperature (1100 °C), the yield strength and hardness
226 of both Mn-containing ODS steels is lower than for *austenitic RT*.

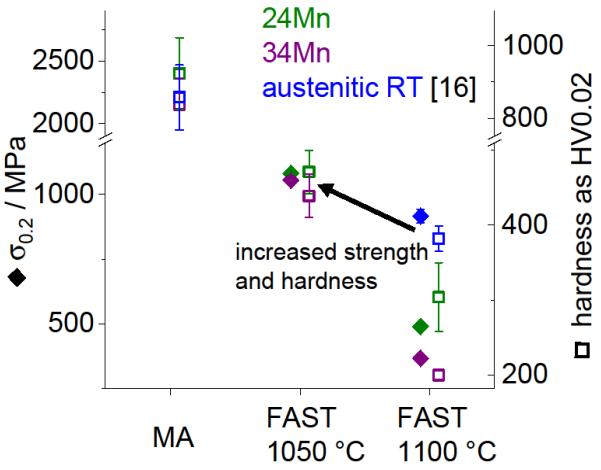

Figure 6: Correlation of yield strength (closed diamonds) and Vickers hardness (open squares) for *24Mn*, *34Mn* and *austenitic RT* (from Ref. [16]) at room temperature for the mechanically alloyed powders as well as after consolidation at 1050 and 1100 °C.

4. Discussion

4.1 Characterization of microstructure

From literature, the FCC lattice parameters for Fe-Mn solid-solutions containing 24 wt.% and 34 wt.% Mn are 3.601 and 3.610 Å, respectively [54]. Corresponding lattice parameters for ε-phase in 24 wt.% Mn-Fe are a = 2.544 Å and c = 4.093 Å [54]. Hence, all determined lattice parameters are in very good agreement with literature expectations. Since the lattice parameters do not change significantly during consolidation, the formation of a homogenous solid solution of Fe and Mn during MA with no further changes in local chemical composition during consolidation can be concluded. Furthermore, BSE micrographs of cross-sections of embedded powder particles (not shown here) confirmed the formation of a homogenous solid solution after MA as well. This is in contrast to the previously investigated Cr-Ni-ODS steel for which the transition to the γ-phase and the formation of a homogenous solid solution only occurred during consolidation [16].

The influence of the consolidation temperature on the consolidation behavior is twofold: (i) The lower limit is determined by the aim to obtain a low porosity after consolidation and (ii) the upper limit is given by the aim to avoid recovery and/or recrystallization to preserve a high dislocation density and ultra-fine grain size. From literature, the solidus temperatures T_s of *24Mn* and *34Mn* are about 1430 and 1390 °C [54], respectively. Hence, the homologous temperatures $T_\mathrm{h} = T \cdot T_\mathrm{s}^{-1}$ are in the range of 0.75 to 0.80 for *24Mn* and 0.77 to 0.83 for *34Mn*, i.e. consolidation of *34Mn* is conducted at comparably higher T_h. Note, that both, Fe self-diffusion and Mn diffusion, is three times and eight times faster at 1050 and 1100 °C compared to 1000 °C, respectively [55]. The relevance of the discussed slight differences in T_h is revealed by the differences in porosity after consolidation (highest porosity for *24Mn-1000*, Fig. S1a) and the larger progress of recrystallization and coarsening determined from the larger grain size of *34Mn-1100* compared to *24Mn-1100*. Hence, the temperature range to obtain

dense but not-substantially recrystallized material to take profit of the non-equilibrium microstructure by MA is small and only includes the consolidation temperature of 1050 °C for the investigated *24Mn* and *34Mn* alloys.

With respect to the absence of ε-phase after consolidation, the XRD results of *34Mn* follow the expectations from literature where no ε-phase was found in high-Mn-containing steels with more than 30 wt.% of Mn [44–46]. In contrast, for cast alloys with 24 wt.% Mn significant fractions of ε-phase of about 40 to 50 vol.% are reported [44,45]. Nevertheless, as indicated by the XRD results, only the partially recrystallized sample of *24Mn* consolidated at 1100 °C exhibits a significant fraction of ε-phase. All other ultra-fine grain sized samples of *24Mn* contain only minor fractions of or no detectable ε-phase. Obviously, the grain size alters the formation of ε-phase, which was already observed by other researchers [47]. Takaki et al. [47] conclude that in grains below 1 µm in diameter only stacking faults form, while the transformation from austenite to ε-phase is not possible. In larger grains up to 20 µm, the formation of ε-phase lamellae with a single preferred orientation per grain is possible [47]. Only in grains larger than 20 to 30 µm in diameter, ε-phase lamellae with different orientations are found [47]. Hence, it can be concluded that in non-recrystallized samples (here *24Mn-MA, 24Mn-1000* and *24Mn-1050*) the grain size is too small (and the dislocation density too high) to form a significant amount of ε-phase, whereas the grain size of recrystallized *24Mn-1100* (> 1 µm) allows for the formation of ε-phase.

4.2 Dislocation density

The Williamson-Hall analysis shows that the main purpose of our work of increasing the dislocation density of austenitic ODS steels by lowering the SFE of alloys is achieved by introducing high-Mn-based ODS steels. In comparison to the Cr-Ni-ODS steel *austenitic RT* from Ref. [16], higher dislocation densities were determined in both Mn-containing ODS steels in all processing steps, e.g. subsequent to MA and after consolidation at 1100 °C (Fig. 2). Note, that consolidation at 1100 °C corresponds to T_h ≈ 0.81 for *austenitic RT*, which is lower than T_h of *34Mn* and comparable to T_h of *24Mn* at the same consolidation temperature which highlights the significance of the higher dislocation density in the Mn-containing alloys. Furthermore, the highest dislocation density in the MA condition was determined in *24Mn*, the alloy with the lowest SFE.

The dislocation density decreases during consolidation due to recovery and/or recrystallization depending on the consolidation temperature. After consolidation at 1000 and 1050 °C where no recrystallization occurs (Fig. S1), dislocation densities of *34Mn* are slightly higher than of *24Mn*. The reason for the higher dislocation densities of *34Mn* remains unsolved, since (i) *24Mn* exhibits a lower SFE according to literature, which should inhibit recovery during consolidation, and (ii) *24Mn* has a higher solidus temperature compared to *34Mn*. Samples of both alloys show enhanced recovery and/or recrystallization during consolidation at 1100 °C (Fig. S1) which is usually accompanied by a

decrease in dislocation density. Nevertheless, in contrast to *34Mn-1100* no drop in dislocation density is observed for *24Mn-1100*, which is expected to result from the accommodation of transformation strain by dislocation formation during the significant formation of ε-phase (Figs. 1 and 3b). This ε-formation was not observed for *24Mn* at lower consolidation temperatures and is completely absent in *34Mn*.

It should be mentioned, that the dislocation density in high-Mn ODS steels can in principle be further increased by the modification of the processing. Apart from differences due to different techniques to obtain the dislocation density, Ashong et al. [48] reported an even one order of magnitude higher density of geometrically necessary dislocations. These were calculated from EBSD kernel average misorientation maps for an ODS steel with 25 wt.% Mn after additional hot rolling of consolidated samples.

4.3 Mechanical properties

In the following discussion of the mechanical properties and strengthening mechanisms, we assume that contributions of Peierls stress and solid solution strengthening are rather similar across the investigated alloys or small in comparison to the dominant mechanisms (dislocation strengthening, Hall-Petch strengthening and Orowan strengthening). Among the MA powders, including the *austenitic RT* powder from Ref. [16], the highest hardness is obtained for *24Mn-MA* which exhibits the lowest SFE and, according to the XRD analysis, the highest dislocation density (Fig. 2). The general drop in hardness and yield strength after consolidation is explained by the annihiliation of dislocations stored in the severly deformed powder after MA as well as by increasing grain size and nanocluster size during consolidation, i.e. contributions from dislocation strengthening, Hall-Petch strengthening and Orowan strengthening decrease.

After consolidation at 1050 °C, the increased hardness and yield strength of the Mn-containing ODS steels compared to *austenitic RT* (consolidated at 1100 °C) is explained by the higher dislocation density of these alloys. EBSD analysis (Figs. 4a and c) as well as APT results (Fig. 5) have shown that grain size, nanocluster size and nanocluster density are in the same range as for *austenitic RT*, i.e. contributions of Hall-Petch strengthening and Orowan strengthening are similar for these alloys.

Contributions of dislocation strengthening can be calculated using the Taylor equation [56]

$$\sigma_{\mathrm{dis}} = \alpha \cdot M \cdot G \cdot b \cdot \sqrt{\rho_{\mathrm{dis}}} \tag{5}$$

in which α is a constant close to 0.2 [57], M is the Taylor factor (about 3.1 [58]), G is the shear modulus (= 81 GPa [59]), b is the Burgers vector (= 0.258 nm [59]) and ρ_{dis} is the dislocation density (taken from XRD analysis). Dislocation strengthening contributions of 222 MPa and 304 MPa are obtained for *24Mn-1050* and *34Mn-1050*, respectively. This is about two to three times higher than in the *austenitic RT* specimen of Ref. [16].

Lower hardness and yield strength is obtained for Mn-containing ODS steels consolidated at 1100 °C. In comparison to consolidation at 1050 °C, (partial) recrystallization occurs for *24Mn-1100* and *34Mn-1100*. This causes substantial grain coarsening (Fig. 3a). Further, it is assumed from the samples annealed at 1100 °C that larger nanoclusters are present in *24Mn-1100* and *34Mn-1100* as well. Hence, contributions of Hall-Petch strengthening and Orowan strengthening decrease in comparison to Mn-containing ODS steels consolidated at 1050 °C, resulting in lower total yield strength when compared to *austenitic RT* [16]. Despite this, the contribution due to dislocation strengthening is still higher in both high-Mn-ODS steels even when recrystallization and grain coarsening occurs. Due to the lower SFE of the high-Mn-ODS steels, the formation of ε-phase is observed in *24Mn-1100*, which favors dislocation nucleation to accommodate transformation strains. Even for *34Mn-1100* for which no phase transformation occurs, suppressed recovery leads to a higher contribution of dislocation strengthening to the yield strength than in *austenitic RT* [16], i.e. the aim to increase the contribution of dislocation strengthening to the yield strength is achieved. Whether *austenitic RT* can be fully consolidated at 1050 °C is unknown so far and needs further investigations. It is assumed that the dislocation density in *austenitic RT* would be lower in comparison to the high-Mn-ODS steels since T_h is similar to *24Mn* and the SFE is much higher. An according contribution to strength is expected.

4.4 Thermal stability

ODS steels are well known for their thermal stability regarding the grain size and the nanocluster size during long-term annealing even at temperatures beyond $0.7 \cdot T_\mathrm{m}$ [27]. In the Cr-Ni-ODS steel *austenitic RT*, almost no coarsening of grains and nanoclusters during long-term annealing at 1000 °C was observed [16]. The same alloy also exhibits stable grain size and nanocluster size after annealing for up to 200 h at 1100 °C (not shown here).

The results of our work confirm the strong influence of nanoclusters on inhibiting grain coarsening and highlight their contribution to the exceptional thermal stability of grain size in Cr-Ni-ODS steels. In consolidated *34Mn*, both, nanocluster size and nanocluster density are in the same order as for *austenitic RT* from Ref. [16]. In contrast to Cr-Ni-ODS steels, nanoclusters in high-Mn-ODS steels coarsen significantly during annealing at 1100 °C. Since nanoclusters are supposed to hinder grain growth by pinning of grain boundaries, the Zener grain size d_Z is calculated as follows [55]:

$$d_\mathrm{Z} = C_\mathrm{Z} \cdot \frac{r_\mathrm{NC}}{f_\mathrm{NC}} \tag{3}$$

C_Z is the Zener constant which is about 1/6 according to Rios [60]. The radius of the nanoclusters r_NC and the volume fraction of the nanoclusters f_NC is obtained from APT data, where f_NC depends on the nanocluster size and density:

$$f_\mathrm{NC} = \frac{4}{3}\pi \cdot r_\mathrm{NC}^3 \cdot \rho_\mathrm{NC} \tag{4}$$

The obtained Zener grain size is about 0.2 µm and 4.4 µm for *34Mn-1050* and *34Mn-1050-HT*, respectively. Although the grain size of *34Mn-1050* could not be determined by EBSD, the calculated value of 0.2 µm seems to be plausible, based on the grain size of the *austenitic RT* alloy in our previous work (0.4 µm, see Ref. [16]) and on other saturation grain size data in MA and consolidated metallic ODS alloys being of similar order [24,61–63]. The Zener grain size of the annealed specimen is in good agreement with the grain size determined by EBSD, especially when the grain size distribution is taken into account. Therefore, it is concluded that the coarsening of nanoclusters leads to an increasing grain size as well.

The coarsening of nanoclusters in high-Mn-ODS steels might be related to the different composition of nanoclusters found in these alloys. From the APT analysis (Fig. 5), it is concluded that the nanoclusters do not consist of ternary $Y_2Ti_2O_7$ as it was proposed for Cr-(Ni-)ODS steels [22,64,65]. Possibly, more complex oxides derived from Y-Mn- or Ti-Mn-oxides are formed during MA and subsequent consolidation. From literature, possible precursors for the nanocluster formation are hexagonal $YMnO_3$ [66], cubic $Y_2Mn_2O_7$ [67,68], orthorhombic YMn_2O_5 [69] or trigonal $MnTiO_3$ [70]. Furthermore, tetragonal $TiMn_2O_4$ was already found in TEM analyses of an Mn-containing ODS steel by Ashong et al. [48], which did not contain any Y. The same authors report on $Y_2Ti_2O_7$, detected by TEM-EDS, but the Fe and Mn signal was neglected in this reference since it was expected to result from the matrix around the nanoclusters.

In the present work, the composition of nanoclusters smaller than about 4 nm in size varies a lot (see also Fig. S2 in the Supplementary). This can be explained by (i) a non-stoichiometric composition of the smallest nanoclusters as it was already proposed in literature [22] or (ii) by an artifact of the atom probe analysis where single missing ions have a strong influence on the composition of nanoclusters consisting of only a few ions. For particles above 4 nm in size, Y and Mn ions possibly substitute each other since the combined concentration of both is constant. Furthermore, the ratio of (Y+Mn):Ti seems to be about 1:1. Hence, possible oxides might be $(Y,Mn)TiO_3$ or $(Y,Mn)_2Ti_2O_7$. For both oxides, the O concentration is above 60 at.%, while only about 40 at.% were determined in the present particles. For the identification of the oxides, e.g. TEM analysis might be necessary in future to determine the crystal structures.

5. Conclusions

The focus of this work was on the characterization of the microstructural and mechanical properties of high-Mn-ODS steels. The aim was to investigate, if the yield strength of the austenitic, Mn-containing ODS steel can be increased in comparison to the formerly published results of a Cr-Ni-containing ODS steel (*austenitic RT*) from Ref. [16] by increasing the dislocation density after consolidation. Therefore, two ODS steels with 24 wt.% or 34 wt.% Mn, respectively, with lower SFE in comparison to Cr-Ni-ODS steels were manufactured by mechanical alloying of elemental powders and subsequent consolidation

by field assisted sintering technique at different consolidation temperatures. The main findings of our work are summarized as follows:

- High-Mn-ODS steels with ultrafine grain size and finely dispersed nanoclusters can be obtained by mechanical alloying and consolidation at 1050 °C. The temperature range for consolidation revealed to be rather small since decreasing the consolidation temperature to 1000 °C led to significant porosity while consolidation at 1100 °C resulted in (partial) recrystallization of both, *24Mn* and *34Mn*.
- Changing the alloy system to high-Mn-ODS steels and thereby decreasing the SFE allowed for increasing the dislocation density after consolidation at all investigated temperatures in comparison to Cr-Ni-ODS steels. Compared to *24Mn*, *34Mn* exhibits higher dislocation densities after consolidation at 1000 and 1050 °C, although the alloy has a higher SFE and a lower solidus temperature.
- When recrystallization occurs (specimens consolidated at 1100 °C), the dislocation density decreases drastically for *34Mn-1100*. Although *24Mn-1100* exhibits recrystallization as well, the material has a similar dislocation density when compared to samples consolidated at lower temperatures. This is explained by the accommodation of strain due to the γ to ε transformation.
- In contrast to *austenitic RT*, where grain size and nanocluster size are stable even after annealing for 200 h at 1100 °C, significant coarsening of grains and nanoclusters is observed in *34Mn-1050-HT* already after annealing at 1100 °C for 1 h. Nanoclusters do not seem to be stable at the recrystallization temperature of high-Mn-containing ODS steels.
- As expected, *34Mn* was single-phase FCC independent of the consolidation temperature and the post heat treatment. In *24Mn* the formation of ε-phase depends on grain size and dislocation density and, hence, the progress of recrystallization during consolidation or heat treatment. Prior to recrystallization the grain size is lower than the critical grain size for the formation of ε-phase. The partially recrystallized specimen *24Mn-1100* revealed about 56 vol.% of ε-phase after consolidation. In *24Mn-1050-HT*, the volume fraction of ε-phase increased remarkably from about 18 vol.% to about 80 vol.% accompanied by grain coarsening during annealing at 1100 °C for 1 h.
- During consolidation, the investigated alloys lose about 50% of their potential hardness due to recovery and/or recrystallization. Nevertheless, it was possible to obtain an austenitic ODS steel with yield strength above 1000 MPa at room temperature which is at least 14% higher than for the formerly investigated *austenitic RT* alloy [16] and which can be related to the impact of dislocation strengthening.

Acknowledgements

The authors acknowledge the financial support through DFG contract no. HE 1872/41-1 and KA 4631/2-1. This work has also received funding from the topic “Materials Research for the Future Energy Supply” within the framework of the Helmholtz Association. This work was partly carried out with the support of the Karlsruhe Nano Micro Facility (KNMF, www.knmf.kit.edu), a Helmholtz Research Infrastructure at Karlsruhe Institute of Technology (KIT, www.kit.edu). We acknowledge G. Schell at IAM-KWT at KIT for the support in sample consolidation. D. Probst is acknowledged for his support in sample preparation.

Data availability statement

The raw data and processed data required to reproduce these findings are available on reasonable request to alexander.kauffmann@kit.edu.

References

[1] S. Ukai, M. Harada, H. Okada, M. Inoue, S. Nomura, S. Shikakura, K. Asabe, T. Nishida, M. Fujiwara, Alloying design of oxide dispersion strengthened ferritic steel for long life FBRs core materials, J. Nucl. Mater. 204 (1993) 65–73.

[2] S. Ukai, M. Harada, H. Okada, M. Inoue, S. Nomura, S. Shikakura, T. Nishida, M. Fujiwara, K. Asabe, Tube manufacturing and mechanical properties of oxide dispersion strengthened ferritic steel, J. Nucl. Mater. 204 (1993) 74–80.

[3] G.R. Odette, Recent Progress in Developing and Qualifying Nanostructured Ferritic Alloys for Advanced Fission and Fusion Applications, JOM. 66 (2014) 2427–2441.

[4] H.S. Cho, A. Kimura, S. Ukai, M. Fujiwara, Corrosion properties of oxide dispersion strengthened steels in super-critical water environment, J. Nucl. Mater. 329–333 (2004) 387–391.

[5] D.T. Hoelzer, B.A. Pint, I.G. Wright, A microstructural study of the oxide scale formation on ODS Fe–13Cr steel, J. Nucl. Mater. 283–287 (2000) 1306–1310.

[6] A. Kimura, R. Kasada, N. Iwata, H. Kishimoto, C.H. Zhang, J. Isselin, P. Dou, J.H. Lee, N. Muthukumar, T. Okuda, M. Inoue, S. Ukai, S. Ohnuki, T. Fujisawa, T.F. Abe, Development of Al added high-Cr ODS steels for fuel cladding of next generation nuclear systems, J. Nucl. Mater. 417 (2011) 176–179.

[7] L.L. Hsiung, M.J. Fluss, S.J. Tumey, B.W. Choi, Y. Serruys, F. Willaime, A. Kimura, Formation mechanism and the role of nanoparticles in Fe-Cr ODS steels developed for radiation tolerance, Phys. Rev. B. 82 (2010) 184103.

[8] A. Alamo, V. Lambard, X. Averty, M.H. Mathon, Assessment of ODS-14%Cr ferritic alloy for high temperature applications, J. Nucl. Mater. 329–333 (2004) 333–337.

[9] I.-S. Kim, J.D. Hunn, N. Hashimoto, D.L. Larson, P.J. Maziasz, K. Miyahara, E.H. Lee, Defect and void evolution in oxide dispersion strengthened ferritic steels under 3.2 MeV Fe+ ion irradiation with simultaneous helium injection, J. Nucl. Mater. 280 (2000) 264–274.

[10] J. Ohta, T. Ohmura, K. Kako, M. Tokiwai, T. Suzuki, Hardness of 12Cr8Mo ferritic steels irradiated by Ni ions, J. Nucl. Mater. 225 (1995) 187–191.

[11] J.H. Schneibel, C.T. Liu, M.K. Miller, M.J. Mills, P. Sarosi, M. Heilmaier, D. Sturm, Ultrafine-grained nanocluster-strengthened alloys with unusually high creep strength, Scr. Mater. 61 (2009) 793–796.

[12] T.-K. Kim, C.-S. Bae, D.-H. Kim, J.-S. Jang, S.-H. Kim, C.-B. Lee, D.-H. Hahn, Microstructural observation and tensile isotropy of an austenitic ODS steel, Nuclear Engineering and Technology. 40 (2008) 305–310.

[13] L. Raman, K. Gothandapani, B.S. Murty, Austenitic Oxide Dispersion Strengthened Steels: A Review, Defence Science Journal. 66 (2016) 316–322.

[14] P. Susila, D. Sturm, M. Heilmaier, B.S. Murty, V.S. Sarma, Microstructural studies on nanocrystalline oxide dispersion strengthened austenitic (Fe–18Cr–8Ni–2W–0.25Y2O3) alloy synthesized by high energy ball milling and vacuum hot pressing, J Mater Sci. 45 (2010) 4858–4865.

[15] H. Peng, F. Song, S. Wang, C. Zhang, Y. Wen, Role of carbon in improving the shape memory effect of Fe–Mn–Si–Cr–Ni alloys by thermo-mechanical treatments, Smart Mater. Struct. 24 (2015) 055010.

[16] S. Seils, A. Kauffmann, F. Hinrichs, D. Schliephake, T. Boll, M. Heilmaier, Temperature dependent strengthening contributions in austenitic and ferritic ODS steels, Materials Science and Engineering: A. 786 (2020) 139452.

[17] J.R.O. Leo, S. Pirfo Barroso, M.E. Fitzpatrick, M. Wang, Z. Zhou, Microstructure, tensile and creep properties of an austenitic ODS 316L steel, Materials Science and Engineering: A. 749 (2019) 158–165.

[18] S. Ukai, M. Fujiwara, Perspective of ODS alloys application in nuclear environments, J. Nucl. Mater. 307 (2002) 749–757.

[19] M.K. Miller, E.A. Kenik, K.F. Russell, L. Heatherly, D.T. Hoelzer, P.J. Maziasz, Atom probe tomography of nanoscale particles in ODS ferritic alloys, Mater. Sci. Eng. A. 353 (2003) 140–145.

[20] C.A. Williams, E.A. Marquis, A. Cerezo, G.D.W. Smith, Nanoscale characterisation of ODS–Eurofer 97 steel: An atom-probe tomography study, J. Nucl. Mater. 400 (2010) 37–45.

[21] M.J. Alinger, G.R. Odette, D.T. Hoelzer, The development and stability of Y–Ti–O nanoclusters in mechanically alloyed Fe–Cr based ferritic alloys, J. Nucl. Mater. 329 (2004) 382–386.

[22] A. Hirata, T. Fujita, Y.R. Wen, J.H. Schneibel, C.T. Liu, M.W. Chen, Atomic structure of nanoclusters in oxide-dispersion-strengthened steels, Nat Mater. 10 (2011) 922–926.

[23] T. Gräning, M. Rieth, J. Hoffmann, S. Seils, P.D. Edmondson, A. Möslang, Microstructural investigation of an extruded austenitic oxide dispersion strengthened steel containing a carbon-containing process control agent, Journal of Nuclear Materials. 516 (2019) 335–346.

[24] C. Balázsi, F. Gillemot, M. Horváth, F. Wéber, K. Balázsi, F.C. Sahin, Y. Onüralp, Á. Horváth, Preparation and structural investigation of nanostructured oxide dispersed strengthened steels, J Mater Sci. 46 (2011) 4598–4605.

[25] C. Heintze, M. Hernández-Mayoral, A. Ulbricht, F. Bergner, A. Shariq, T. Weissgärber, H. Frielinghaus, Nanoscale characterization of ODS Fe–9%Cr model alloys compacted by spark plasma sintering, J. Nucl. Mater. 428 (2012) 139–146.

[26] Y. Miao, K. Mo, Z. Zhou, X. Liu, K.-C. Lan, G. Zhang, M.K. Miller, K.A. Powers, Z.-G. Mei, J.-S. Park, J. Almer, J.F. Stubbins, On the microstructure and strengthening mechanism in oxide dispersion-strengthened 316 steel: A coordinated electron microscopy, atom probe tomography and in situ synchrotron tensile investigation, Materials Science and Engineering: A. 639 (2015) 585–596.

[27] J.H. Schneibel, M. Heilmaier, W. Blum, G. Hasemann, T. Shanmugasundaram, Temperature dependence of the strength of fine- and ultrafine-grained materials, Acta Mater. 59 (2011) 1300–1308.

[28] J.H. Schneibel, M. Heilmaier, Hall-Petch Breakdown at Elevated Temperatures, Mater. Trans. 55 (2014) 44–51.

[29] B.P. Kashyap, Towards interrelationship of grain size, cell parameters and flow stress in type 316L stainless steel, Acta Materialia. 50 (2002) 2413–2427.

[30] S. Takaki, K. Kawasaki, Y. Kimura, Mechanical properties of ultra fine grained steels, Journal of Materials Processing Technology. 117 (2001) 359–363.

[31] C.G. Rhodes, A.W. Thompson, The composition dependence of stacking fault energy in austenitic stainless steels, MTA. 8 (1977) 1901–1906.

[32] T. Yonezawa, K. Suzuki, S. Ooki, A. Hashimoto, The Effect of Chemical Composition and Heat Treatment Conditions on Stacking Fault Energy for Fe-Cr-Ni Austenitic Stainless Steel, Metall Mater Trans A. 44 (2013) 5884–5896.

[33] H. Schumann, Einfluß der Stapelfehlerenergie auf den kristallographischen Umgitterungsmechanismus der γ/α-Umwandlung in hochlegierten Stählen, Kristall und Technik. 9 (1974) 1141–1152.

[34] D.T. Pierce, J.A. Jiménez, J. Bentley, D. Raabe, C. Oskay, J.E. Wittig, The influence of manganese content on the stacking fault and austenite/ε-martensite interfacial energies in Fe–Mn–(Al–Si) steels investigated by experiment and theory, Acta Materialia. 68 (2014) 238–253.

509 [35] R.E. Schramm, R.P. Reed, Stacking fault energies of seven commercial austenitic stainless steels,
510 MTA. 6 (1975) 1345.
511 [36] J. Kim, S.-J. Lee, B.C. De Cooman, Effect of Al on the stacking fault energy of Fe–18Mn–0.6C
512 twinning-induced plasticity, Scripta Materialia. 65 (2011) 363–366.
513 [37] M. Kang, W. Woo, Y.-K. Lee, B.-S. Seong, Neutron diffraction analysis of stacking fault energy in
514 Fe–18Mn–2Al–0.6C twinning-induced plasticity steels, Materials Letters. 76 (2012) 93–95.
515 [38] J.S. Jeong, W. Woo, K.H. Oh, S.K. Kwon, Y.M. Koo, In situ neutron diffraction study of the
516 microstructure and tensile deformation behavior in Al-added high manganese austenitic steels,
517 Acta Materialia. 60 (2012) 2290–2299.
518 [39] L. Remy, Temperature variation of the intrinsic stacking fault energy of a high manganese
519 austenitic steel, Acta Metallurgica. 25 (1977) 173–179.
520 [40] X. Tian, Y. Zhang, Effect of Si content on the stacking fault energy in γ-Fe–Mn–Si–C alloys: Part I.
521 X-ray diffraction line profile analysis, Materials Science and Engineering: A. 516 (2009) 73–77.
522 [41] G.B. Olson, M. Cohen, A general mechanism of martensitic nucleation: Part I. General concepts
523 and the FCC → HCP transformation, MTA. 7 (1976) 1897–1904.
524 [42] Y.-K. Lee, C. Choi, Driving force for γ→ε martensitic transformation and stacking fault energy of
525 γ in Fe-Mn binary system, Metall Mater Trans A. 31 (2000) 355–360.
526 [43] A. Saeed-Akbari, J. Imlau, U. Prahl, W. Bleck, Derivation and Variation in Composition-Dependent
527 Stacking Fault Energy Maps Based on Subregular Solution Model in High-Manganese Steels,
528 Metall and Mat Trans A. 40 (2009) 3076–3090.
529 [44] A. Holden, J.D. Bolton, E.R. Petty, Structure and properties of iron-manganese alloys, Journal of
530 the Iron and Steel Institute. 209 (1971) 721–728.
531 [45] Y. Tomota, M. Strum, J.W. Morris, Microstructural dependence of Fe-high Mn tensile behavior,
532 Metall Mater Trans A. 17 (1986) 537–547.
533 [46] A.P. Gulyaev, T.F. Volynova, I.Ya. Georgieva, Phase transformations in high-purity Fe−Mn alloys,
534 Met Sci Heat Treat. 20 (1978) 179–182.
535 [47] S. Takaki, H. Nakatsu, Y. Tokunaga, Effects of Austenite Grain Size on ε Martensitic
536 Transformation in Fe-15mass%Mn Alloy, Materials Transactions, JIM. 34 (1993) 489–495.
537 [48] A.N. Ashong, M.Y. Na, H.C. Kim, S.H. Noh, T. Park, H.J. Chang, J.H. Kim, Influence of manganese
538 on the microstructure and mechanical properties of oxide-dispersion-strengthened steels,
539 Materials & Design. 182 (2019) 107997.
540 [49] D. Vaumousse, A. Cerezo, P.J. Warren, A procedure for quantification of precipitate
541 microstructures from three-dimensional atom probe data, Ultramicroscopy. 95 (2003) 215–221.

[50] A. Heinrich, T. Al-Kassab, R. Kirchheim, Investigation of the early stages of decomposition of Cu–0.7at.% Fe with the tomographic atom probe, Materials Science and Engineering: A. 353 (2003) 92–98.

[51] E.A. Marquis, J.M. Hyde, Applications of atom-probe tomography to the characterisation of solute behaviours, Materials Science and Engineering: R: Reports. 69 (2010) 37–62.

[52] J.B. Nelson, D.P. Riley, An experimental investigation of extrapolation methods in the derivation of accurate unit-cell dimensions of crystals, Proc. Phys. Soc. 57 (1945) 160.

[53] G.K. Williamson, W.H. Hall, X-ray line broadening from filed aluminium and wolfram, Acta Metallurgica. 1 (1953) 22–31.

[54] B. Predel, Fe-Mn (Iron-Mangenese), in: O. Madelung (Ed.), Phase Equilibria, Crystallographic and Thermodynamic Data of Binary Alloys · Dy-Er – Fr-Mo, Springer-Verlag, Berlin/Heidelberg, 1995: pp. 1–8.

[55] C.S. Smith, Grains, phases, and interfaces - An interpretation of microstructure, Transactions of the American Institute of Mining and Metallurgical Engineers. 175 (1948) 15–51.

[56] G.I. Taylor, The mechanism of plastic deformation of crystals. Part I. Theoretical, Proceedings of the Royal Society of London Series A. 145 (1934) 362–387.

[57] H. Wiedersich, Hardening mechanisms and the theory of deformation, JOM. 16 (1964) 425–430.

[58] W.F. Hosford, Mechanical Behavior of Materials, in: Cambridge University Press, Cambridge, 2005: p. 31.

[59] H.J. Frost, M.F. Ashby, Deformation-Mechanism Maps: the Plasticity and Creep of Metals and Ceramics, in: Pergamon Press, Oxford, 1982: pp. 62–63.

[60] P.R. Rios, A theory for grain-boundary pinning by particles, Acta Metallurgica. 35 (1987) 2805–2814.

[61] Z. Li, L. Chen, H. Zhang, S. Zhang, Z. Zhang, Effect of annealing temperature on microstructure and mechanical properties in oxide dispersion strengthened Fe-14Cr alloys prepared by spark plasma sintering, Mater. Res. Express. 6 (2019) 126515.

[62] H. Saage, M. Heilmaier, J. Eckert, On the Orowan stress in intermetallic ODS alloys and its superposition with grain size and solid solution hardening, MEKU. 96 (2005) 801–806.

[63] D.V. Kudashov, H. Baum, U. Martin, M. Heilmaier, H. Oettel, Microstructure and room temperature hardening of ultra-fine-grained oxide-dispersion strengthened copper prepared by cryomilling, Materials Science and Engineering: A. 387–389 (2004) 768–771.

[64] K. Oka, S. Ohnuki, S. Yamashita, N. Akasaka, S. Ohtsuka, H. Tanigawa, Structure of nano-size oxides in ODS steels and its stability under electron irradiation, Mater. Trans. 48 (2007) 2563–2566.

576 [65] M.C. Brandes, L. Kovarik, M.K. Miller, M.J. Mills, Morphology, structure, and chemistry of
577 nanoclusters in a mechanically alloyed nanostructured ferritic steel, J Mater Sci. 47 (2012) 3913–
578 3923.
579 [66] H.L. Yakel, W.C. Koehler, E.F. Bertaut, E.F. Forrat, On the crystal structure of the manganese(III)
580 trioxides of the heavy lanthanides and yttrium, Acta Cryst. 16 (1963) 957–962.
581 [67] M.A. Subramanian, C.C. Torardi, D.C. Johnson, J. Pannetier, A.W. Sleight, Ferromagnetic
582 R2Mn2O7 pyrochlores (R = Dy-Lu, Y), Journal of Solid State Chemistry. 72 (1988) 24–30.
583 [68] Y. Shimakawa, Y. Kubo, N. Hamada, J.D. Jorgensen, Z. Hu, S. Short, M. Nohara, H. Takagi, Crystal
584 structure, magnetic and transport properties, and electronic band structure of A2Mn2O7
585 pyrochlores (A= Y, In, Lu, Tl), Phys. Rev. B. 59 (1999) 1249–1254.
586 [69] I. Kagomiya, K. Kakimoto, H. Ohsato, Precursor phenomenon on ferroelectric transition in
587 multiferroic YMn2O5, Journal of the European Ceramic Society. 30 (2010) 255–258.
588 [70] K. Kidoh, K. Tanaka, F. Marumo, H. Takei, Electron density distribution in ilmenite-type crystals.
589 II. Manganese(II) titanium(IV) trioxide, Acta Cryst B. 40 (1984) 329–332.